Finite-Difference Time-Domain Simulation of Strong-Field Ionization

A Perfectly Matched Layer Approach

Kamban, Høgni C.; Christensen, Sigurd S.; Søndergaard, Thomas; Pedersen, Thomas G.

Published in:
Physica Status Solidi (B) Basic Research

DOI (link to publication from Publisher):
10.1002/pssb.201900467

Publication date:
2020

Document Version
Accepted author manuscript, peer reviewed version

Finite-difference time-domain simulation of strong-field ionization: Perfectly matched layer approach

Høgni C. Kamban,[1,2,*] Sigurd S. Christensen,[1] Thomas Søndergaard,[1] and Thomas G. Pedersen[1,2]

[1] *Department of Materials and Production, Aalborg University, DK-9220 Aalborg Øst, Denmark*

[2] *Center for Nanostructured Graphene (CNG), DK-9220 Aalborg Øst, Denmark*

(Dated: February 3, 2020)

* hck@mp.aau.dk

A Finite-Difference Time-Domain (FDTD) scheme with Perfectly Matched Layers (PMLs) is considered for solving the time-dependent Schrödinger equation, and simulate the laser induced ionization of two systems: (i) an electron initially bound to a one-dimensional δ-potential, and (ii) excitons in carbon nanotubes (CNTs). The performance of PMLs based on different absorption functions are compared, where we find slowly growing functions to be preferable. PMLs are shown to be able to reduce the computational domain, and thus the required numerical resources, by several orders of magnitude. This is demonstrated by testing the proposed method against an FDTD approach without PMLs and a very large computational domain. We further show that PMLs outperform the well known Exterior Complex Scaling (ECS) technique for short-range potentials when implemented in FDTD. For long-range potentials such as in CNTs, however, ECS performs better than PMLs when propagating over many periods.

This article has been accepted for publication and undergone full peer review but has not been through the copyediting, typesetting, pagination and proofreading process, which may lead to differences between this version and the Version of Record. Please cite this article as doi: 10.1002/pssb.201900467

I. Introduction

It has long been established that excitons must be taken into account to accurately describe the optical properties of non-metallic solids. In fact, with the increased interest in low-dimensional solids, understanding excitonic effects becomes even more important, as the reduced screening in low-dimensional semiconductors leads to excitons with extremely large binding energies. Of particular interest have been two-dimensional (2D) transition metal dichalcogenides (TMDs) and one-dimensional (1D) carbon nanotubes (CNTs). 2D TMDs are known to support exciton binding energies of up to several hundred meVs [1–3], and exciton binding energies in CNTs can be larger still for tubes with small radii [4, 5]. These strongly bound excitons dominate the absorption spectra of both TMDs [6, 7] and CNTs [8–11]. Monolayer TMDs have been shown to absorb a large amount of sunlight relative to their thickness [12], which makes them interesting building blocks in solar cells and other photocurrent devices [12, 13]. However, to produce a photocurrent in these devices, the excitons must be dissociated into free electrons and holes. Whereas excitons in bulk semiconductors can usually be dissociated efficiently by thermal agitation, the strongly bound excitons in lower-dimensional structures can not. Recently, applying a static in-plane electric field over the TMDs as a means of inducing dissociation has gained interest [7, 14, 15]. Similarly, the large exciton binding energy in semiconducting CNTs makes it difficult to generate a photocurrent [16]. Static field induced exciton dissociation rates in CNTs have been studied both theoretically [17] and experimentally [18–20], and may contribute, e.g., to photoconductivity [18].

In the present paper, we are interested in computing exciton dissociation induced by time-dependent electric fields, i.e., laser fields. One of the most reliable techniques of obtaining

accurate results in intense laser-matter interactions is to propagate the time-dependent Schrödinger equation (TDSE) and calculate the relevant observables. Strong electric fields lead to a large probability flux traveling out of the central region occupied by the initially localized wave function, which, of course, is exactly what we mean by ionization. If one simply uses Dirichlet boundary conditions at the edges of the simulation domain, a huge domain is required to avoid reflections of the wave function from the boundary. Several methods have been designed to circumvent this problem, with one of the most common ones being absorbing boundaries outside a specified interior domain. Popular methods include complex absorbing potentials (CAPs) [21], absorbing masks [22], and exterior complex scaling (ECS) [23, 24]. The goal of the absorbing layers is to leave the wave function unaltered in the interior region, while absorbing it as it moves out of this region. If it is absorbed sufficiently quickly, then one is able to use Dirichlet boundary conditions at a distance into the layer with minimal flux reaching this point and thus avoiding spurious reflections.

The ECS method has been given a lot of attention in recent years, and rightfully so, as it has been shown to be a very efficient absorber in time-dependent Schrödinger problems [25, 26]. A related method that has been given less attention in quantum mechanics is the use of PMLs. The PML method was developed by Berenger for solving Maxwell's equations [27], and has since been used extensively in classical electromagnetism, where PMLs are applied efficiently in FDTD [28, 29], in frequency-domain finite-element [30], and in Fourier-series [31] approaches. Lu and Zhu additionally proposed a perturbative approach [32] to deal with undesired effects of the PML when simulating optical wave guides, and PMLs have, furthermore, been utilized to study sound waves [33]. Given the success of the PML method in solving problems in electromagnetism, interest in applying it to Schrödinger problems has slowly been increasing.

Zheng used it to solve the nonlinear Schroödinger equation [34], and Nissen and Kreiss have since tried to optimize the PML method for the Schrödinger equation with time-independent potentials [35], and have, together with Karlsson, applied it to a reactive scattering problem [36]. PMLs have also been applied to time-dependent-density-functional theory (TDDFT) [37], and the Dirac equation [38]. It is, however, surprising how comparatively little work has been done on applying PMLs in Schrödinger problems, in particular, for explicitly time-dependent problems, such as intense laser-matter interactions.

In the present paper, we develop a method based on a finite-difference time-domain (FDTD) scheme including a PML to describe dissociation of excitons in CNTs. The focus of the paper is therefore twofold: (i) To compute the laser-induced dissociation rates, and (ii) to compare the accuracy of the PML method to the well known ECS method. We therefore begin by describing the methodology behind absorbing layers, and describe how they are imposed in the two methods. As a preliminary, we proceed by analyzing a zero-range potential. This potential has previously been used to, e.g., study the optical response in one-dimensional semiconductors [39] and to model ionization of the H^- ion [40]. The motivation for analyzing the zero-range potential is that it is sufficiently simple that analytical results are available in limiting cases. It may therefore be used to ensure that the methods work as intended. We thereafter turn to analyze the interaction between CNT excitons and a laser field, and in so doing, we again compare the accuracy of the PML method to that of ECS.

II. Time-dependent Schrödinger with a Laser Field

As will be discussed later, the exciton problem may reformulated as a Schrödinger type

problem. We therefore begin by setting up the Schrödinger problem quite generally. The time-dependent Schrödinger equation perturbed by a laser field reads (in atomic units)

$$i\frac{d}{dt}\psi(\boldsymbol{r},t)=\left[-\frac{1}{2}\nabla^2+H_g(\boldsymbol{r},t)+V(\boldsymbol{r})\right]\psi(\boldsymbol{r},t), \tag{1}$$

where H_g describes the interaction induced by the laser field. Here, the subscript g refers to the gauge, in which the interaction is considered. We shall work only in the dipole approximation such that neither electric fields nor vector potentials have any spatial dependence. This leads to the interaction in the velocity gauge (VG) being

$$H_V=\boldsymbol{p}\cdot\boldsymbol{A}(t), \tag{2}$$

where $\boldsymbol{p}$ is the momentum operator and $\boldsymbol{A}$ is the vector potential. Note that the usual $A(t)^2/2$ term has been removed by a unitary transformation. We will consider the monochromatic field defined by

$$\boldsymbol{A}(t)=A_0\cos(\omega t)\hat{\boldsymbol{x}}. \tag{3}$$

In the length gauge (LG), the interaction is given in terms of the electric field

$$\mathbf{E}(t)=-\frac{\partial\boldsymbol{A}(t)}{\partial t}=\mathsf{E}_0\sin(\omega t)\hat{\boldsymbol{x}} \tag{4}$$

by

$$H_L=\boldsymbol{r}\cdot\mathbf{E}(t). \tag{5}$$

When introducing absorbing layers into the Schrödinger equation, the goal is to be able to reproduce the exact wave function in an interior box $|\boldsymbol{r}|\le R_0$ for relevant time periods. One therefore seeks to modify the TDSE so that the solution to the modified equation ψ satisfies

$$\psi(\boldsymbol{r},t)=\psi_{\mathrm{ex}}(\boldsymbol{r},t)\quad\text{for}\,|\boldsymbol{r}|\le R_0, \tag{6}$$

where ψ_{ex} is the exact wave function. To be able to quantify the error between the exact and

approximate wave functions by a single number, the error measurement introduced by Scrinzi [26] will be used

$$\sigma(R_0) = 1 - \frac{\left|\left\langle \psi_{ex} \mid \psi \right\rangle_{R_0}\right|^2}{\left\langle \psi_{ex} \mid \psi_{ex} \right\rangle_{R_0} \left\langle \psi \mid \psi \right\rangle_{R_0}}, \tag{7}$$

where the scalar product is to be taken in the region $|\boldsymbol{r}| \leq R_0$, i.e.

$$\left\langle f \mid g \right\rangle_{R_0} = \int_{|\boldsymbol{r}| \leq R_0} f^*(\boldsymbol{r})\, g(\boldsymbol{r})\, d\boldsymbol{r}. \tag{8}$$

III. Exterior Complex Scaling

The literature covering complex scaling is vast (see e.g. [41–46] and references therein), and for this reason we shall only describe briefly the most relevant aspects to the present paper before describing how PMLs are implemented. For simplicity, we will restrict the discussion to one dimension x. The simplest form of complex scaling is implemented by scaling the coordinates uniformly according to $x \to xe^{i\theta}$, where θ will be taken as a purely real number. The motivation is that the outgoing waves $\exp(ikx)$ become exponentially decaying waves if the rotational angle θ is chosen large enough. This transformation, referred to as uniform complex scaling (UCS), has been used with great success in finding ionization rates for static electric fields [7, 47, 48] and in solving the TDSE [46]. In certain situations, however, one may wish to leave the domain untransformed in an interior region and introduce complex scaling only in an outer region. The original motivation was that UCS cannot be used with the Born-Oppenheimer approximation [49]. Furthermore, when dealing with sufficiently weak electric fields, ionization rates typically become so low that UCS results in a wave function that (numerically) vanishes

before it reaches the important region far from the core [15]. The ECS [25, 49–51] procedure circumvents these problems, and is implemented in one dimension by the transformation

$$x \to \tilde{x} = \begin{cases} x & \text{for} \left| x \right| < R_0 \\ e^{i\theta}\left(x \pm R_0 \right) \mp R_0 & \text{for} \mp x > R_0 , \end{cases} \tag{9}$$

where R_0 is referred to as the scaling radius. This transformation turns outgoing waves into decaying waves in the absorbing layer while leaving them unaffected in the interior region.

The resulting behaviour of the wave function in the absorbing layer is slightly different in the two gauges. The exponential propagator can be constructed as usual (see Ref. [23]), and the perturbing part can be written as

$$\exp\left(-iH_L \Delta t \right) = \exp\left\{ -i\mathsf{E}(t)\left[\cos\theta \left(x \pm R_0 \right) \mp R_0 \right] \Delta t \right\}$$

$$\times \exp\left\{ \mathsf{E}(t) \sin\theta \left(x \pm R_0 \right) \Delta t \right\}, \tag{10}$$

in LG and as

$$\exp\left(-iH_V \Delta t \right) = \exp\left(-i\cos\theta A(t) p_x \Delta t \right)$$

$$\times \exp\left(-\sin\theta A(t) p_x \Delta t \right), \tag{11}$$

in VG. The first terms on the right-hand sides of Eqs. (10) and (11) are oscillatory, while the second terms are either exponentially increasing or exponentially decreasing. In LG, this depends on the sign of the oscillatory field $\mathsf{E}(t)$ and in VG on the sign of $A(t)$. Thus, in both cases one may obtain an undesired exponentially increasing behavior in the absorbing layer. Given that the behavior depends on the sign of the field or vector potential, the propagators will oscillate between amplifying and damping the wave function exponentially. In practice, we have found that the exponential behavior outside of the scaling radius is much more apparent in LG than inVG. Furthermore, in LG, the exponential behavior is more volatile for larger x, which may lead to numerical instabilities if a wide absorbing layer is desired. In practice, we have not found

these growing terms to cause numerical instabilities for moderate frequencies, while for low frequencies they lead to a numerically diverging wave function. This is in agreement with the observations in Ref. [23].

IV. Perfectly Matched Layers

The PML scheme for the TDSE is usually derived by assuming that the potential is both spatially and temporally invariant, and then modal analysis is performed on the Laplace-transformed equation to ensure that the solution decays outside the interior domain, i.e. $|x| > R_0$ [34–36]. The transformation can be formulated as

$$x \to \tilde{x} = \begin{cases} x & \text{for} |x| < R_0 \\ x + i\sigma_0 \int^{x} f(x')\,dx' & \text{for} [x] > R_0, \end{cases} \tag{12}$$

where σ_0 is a constant referred to as the absorption strength and f is the absorption function. The absorption function is zero inside the interior $|x| \le R_0$ and positive otherwise. Specific forms will be discussed later. Unlike in ECS, the transformation in Equation (12) is not applied to the potential. Thus, the PML method can be understood as a transformation of the differential operator

$$\frac{\partial}{\partial x} \to c(x)\frac{\partial}{\partial x}, \tag{13}$$

where $c(x) = 1/\left[1 + i\sigma_0 f(x)\right]$. The PML equation in one dimension therefore becomes

$$i\frac{\partial}{\partial t}\psi = \left[-\frac{1}{2}c(x)\frac{\partial}{\partial x}c(x)\frac{\partial}{\partial x} + H_g(x,t) + V(x)\right]\psi, \tag{14}$$

which coincides with the usual TDSE inside a box of radius R_0 as $c(|x| \le R_0) = 1$. Note that the

momentum operator in H_V (see Equation(2)) is also transformed according to Equation (13). As the transformation is only applied to the spatial derivatives, it is only reasonable to expect Eq. (14) to yield a good approximation if R_0 is chosen sufficiently large so that the variations in the potential $V(x)$ in the exterior are negligible. This is the case for any non-zero R_0 for the zero-range potential $V(x) = -\delta(x)$. However, the interaction in LG effectively modifies the potential so that it includes a linear term which does not vanish outside the interior. One may therefore speculate to which degree Equation (14) in LG is able to approximate the exact wave function in the interior. Indeed, as we show numerically below, implementing the PML in LG introduces significantly larger errors than in VG. The ECS and PML methods have been implemented using a Crank-Nicolson (CN) finite difference scheme. The technical details can be found in Appendix A.

While the following analysis is made for effectively one-dimensional systems, generalization of PMLs to cases of higher dimensions is straightforward. One simply transforms the spatial derivatives in the x-, y-, and z-directions independently as in Equation (13). The absorption functions need not be identical, and it is therefore possible to control the rate of absorption in different directions. When implemented in more than one dimension, it is advantageous to use the alternating direction implicit (ADI) method combined with Strang's splitting technique [34].

A. Absorption function

It is important that the absorption function f be chosen positive to ensure decay of the wave function as it travels out of the interior domain. Previous choices include low-degree power

functions [27, 34] and singular functions [52]. It is interesting to examine whether or not there is a substantial difference between the numerical accuracy obtainable with the different functions. To this end, we will compare four different absorption functions, namely

$$f(y) = \Theta(y)\begin{cases} d\left(d - y + \epsilon\right)^{-1} - 1 \\ y^2 \\ y^3 \\ \tanh\left(2yd^{-1} - 1\right) - \tanh(-1), \end{cases} \tag{15}$$

where $y = |x| - R_0$, ϵ is some small positive number, and Θ is a step function equal to unity for $y \geq 0$ and zero otherwise, and d is the width of the absorbing layer. For ϵ, we have used 10^{-4}, as we have not found the results to be highly dependent on ϵ.

V. Zero-range Potential

The zero-range potential $-\delta(x)$ serves as a good check that the methods introduced behave as expected. The reason is that it is sufficiently simple that analytical results may be obtained in limiting cases, and we are therefore able to compare the numerical results to already known results. As expressing the exact $-\delta$ potential is not feasible in a finite-difference scheme, we approximate it by

$$V(x) = \begin{cases} -\dfrac{1}{2b} & \text{for } |x| < b, \\ 0 & \text{otherwise.} \end{cases} \tag{16}$$

We have used $b = 5 \times 10^{-3}$ for the calculations in the present paper, which leads to a ground-state energy of $E_0 = -0.4967$ a.u. (as opposed to $-1/2$ a.u. for the zero-range potential).

A. Error analysis

To illustrate the effect of absorbing layers on the wave function, as well as the temporal oscillations outside R_0 when implementing ECS in LG that were discussed briefly in the ECS section above, we show the absolute square of the wave function in Figure 1 at three different times. The oscillations are immediately clear. The absolute square of the wave function is, however, graphically indistinguishable in the interior for ECS implemented in LG and VG. For the PML calculations, the results are not as equal-footed. The LG calculation introduces non-negligible reflections leading to a large error inside the interior. This is, of course, what we seek to avoid and thus one must be careful in implementing PML in LG. For VG, the PML and ECS wave functions are indistinguishable for $|x| \leq R_0$.

To perform error analysis, we need a reference function. It was obtained by calculating the error in Equation (7) inside $R_0 = 20$ a.u. at $t = 200$ a.u. between two wave functions without any transformation and with Dirichlet boundary conditions set at $x = \pm n \times 500$ for ψ and $x = \pm (n+1) \times 500$ a.u. for ψ_{ex}, where n is a positive integer, which was increased by one until the error vanished within numerical precision. This occurred at $n = 8$, and thus without any absorbing layer a domain width of at least 8000 a.u. is needed. To ensure a numerically exact reference function, we have used a domain width of 10000 a.u. for ψ_{ex} in the error calculations. In Figure 2 we show the error calculated by Equation (7) at $t = 200$ a.u. as a function of the PML width d for the different absorption functions with various absorption strengths σ_0. It is clear that the PML should be implemented in VG to obtain an accurate wave function in the interior. We also notice that an absorption function that grows slowly leads to a lower error at the cost of slower convergence. The reason is that less of the wave function will be (numerically) reflected

upon entering the absorbing layer when the transition is more gradual. The error introduced by the power functions converge to a constant value for a sufficiently large d. This indicates that the entire outgoing flux has either been absorbed or reflected from the layer, and further increasing d does not make any difference. It is worth noting that the PML method with a quadratic absorption function (Figure 2(b)) leads to errors of order 10^{-15} for an absorbing layer of around $d = 40$ a.u.. Thus, the domain width required to obtain an excellent approximation to the exact wave function is $2(d + R_0) = 120$ a.u., significantly lower than the domain width of 8000 a.u. needed without any absorbing layer. As the calculation scales directly with the number of points used to describe the entire domain (physical + absorbing), this results in a significant computational speed-up. To obtain a short computational time, it is therefore desirable to choose the box size, PML width, and σ_0 such that the entire domain becomes as small as possible, while ensuring that the errors introduced are not too large. For the nearly singular function and the $\tanh$ function, increasing d leads to an absorption function that grows more slowly. For this reason, the errors they induce do not converge in the same manner as those induced by the power functions. Rather, they continue to decrease as the absorbing layers become wider. The PML errors should be compared to those introduced by the ECS method, shown in Figure 3, for which both LG and VG calculations converge to the same error, and are nearly indistinguishable. A low rotational angle θ can be seen to introduce lower errors, as less of the wave function will be reflected upon entering the absorbing layer, exactly as with the PML method. By comparing the errors introduced by ECS to those for PMLs with a quadratic absorption function in Figure 2(b), we see that the ECS errors for comparable absorption widths converge to values that are around six orders of magnitude larger. For PMLs with a cubic absorption function (Figure 2(c)), the ECS errors are around four orders of magnitude larger. This might be due to the poor

performance of ECS when implemented in finite-difference schemes [50]. The same behavior is observed in Figure 4, where the error is shown as a function of time. The PML LG calculation introduces much larger errors than the other two methods, and the ECS LG and VG errors are graphically indistinguishable. Again, the PML VG calculation leads to the lowest error by several orders of magnitude. The dashed lines show a scaling radius of $R_0 = 10$ a.u. as opposed to $R_0 = 20$ a.u.. As can be seen, reducing the size of the box does not have a large impact on the errors in the interior domain, and particularly not for ECS.

B. Polarizability and ionization

In the previous section, the error of the wave function inside the box $|x| < R_0$ was analyzed. If the wave function can be reproduced, then the desirable observables can be calculated, as long as the box size is chosen adequately. While the error measurement defined by Equation (7) is a meaningful parameter, we are unable to directly relate it to physical observables. As an additional check, we therefore demonstrate that we are able to reproduce the frequency dependent polarizability in the weak-field limit. Numerically, the polarizability α can be found by calculating $\langle x \rangle / \mathsf{E}_0$ in the weak field limit, and relating it to the real and imaginary part of α. Here, $\langle x \rangle$ is the expectation value of x. As the field amplitude is extremely low, and $\langle x \rangle$ is only needed over a single period, the integral in $\langle x \rangle$ can, to an excellent approximation, be restricted to the interior region. An analytical expression can be found for α of the δ-potential ground-state using linear perturbation theory [53]. It is given by

$$\alpha(\omega) = \frac{2 - \omega^2 - \sqrt{1 + 2\omega} - \sqrt{1 - 2\omega}}{\omega^4}. \tag{17}$$

As can be seen in Figure 5, the PML simulations using a low field strength of $\mathsf{E}_0 = 10^{-6}$ a.u. are in

excellent agreement with the analytical results.

A special interest in the present paper is to obtain the strong-field ionization rate. The probability of occupying a bound state (that is, not being ionized) can be found by

$$P_{\text{bound}}(t;\mathsf{E}_0) = \sum_b \left|\left\langle \varphi_b \mid \psi_{\text{ex}} \right\rangle\right|^2, \tag{18}$$

where the sum is to be taken over all bound states. For numerical calculations, however, one may cut the sum after convergence to a desired number of digits. Let us denote the most delocalized state included in the sum by φ_B, such that from some number L

$$\left|\varphi_B(x)\right| \geq \left|\varphi_b(x)\right| \quad \text{for} \left|x\right| \geq L, \tag{19}$$

where b refers to all states included. If L is chosen such that φ_B is negligible for $|x| > L$, then all integrals in Equation (18) may be restricted to $|x| < L$. By choosing the scaling radius R_0 to coincide with L, we can therefore describe all bound states, as well as obtain an excellent approximation to the wave function, in the interior domain, allowing us to implement Equation (18) in the present approach. For the short-range potential defined by Equation (16) there is only one bound state and it decays exponentially for $|x| > b$. Therefore, a scaling radius of $R_0 = 20$ a.u. is expected to be adequate. The probability of not being ionized can be seen as a function of time in Figure 6, where the ECS and PML calculations are compared to a converged Crank-Nicolson calculation in an untransformed domain. As is evident, the result obtained by the PML method in LG is the only one that can be distinguished from the other ones. This is yet another indication that care must be taken when implementing PMLs in LG.

To obtain the time-dependent ionization rate Γ, we use

$$\Gamma(t;\mathsf{E}_0) = -\frac{d}{dt}\ln P_{\text{bound}}(t;\mathsf{E}_0). \tag{20}$$

The ionization rate defined by Equation (20) will oscillate in time. It is therefore convenient to average the time-dependent ionization rate over a number of periods to remove these oscillations, and thereby obtain a time-independent ionization rate, i.e.

$$\left\langle \Gamma(\mathsf{E}_0) \right\rangle = \frac{\omega}{2n\pi} \int_{t_0}^{t_0 + 2n\pi/\omega} \Gamma(t; \mathsf{E}_0)\, dt, \tag{21}$$

where n is the number of periods, and t_0 is an initial time taken after the field has been turned on. The ionization rate averaged over two periods can be seen in the upper panel of Figure 7 for $\omega = 0.2$ a.u.. As is evident, the four methods yield identical results. Furthermore, the shape of the ionization rate is consistent with the results for three-photon ionization in Ref. [40].

In the adiabatic limit, one can obtain analytical results for the ionization rate of the zero-range potential. By setting up the Schrödinger equation for a static electric field $\mathsf{E}_{\mathrm{DC}} > 0$ and requiring that the wave function becomes an outgoing wave as $x \to -\infty$ [54], one can obtain the following condition

$$\frac{\mathsf{E}_{\mathrm{DC}}^{1/3}}{2^{2/3}\pi} - \mathrm{Ai}(\lambda)\mathrm{Bi}(\lambda) = i\mathrm{Ai}^2(\lambda), \tag{22}$$

where $\lambda = -2^{1/3} E \mathsf{E}_{\mathrm{DC}}^{-2/3}$, and Ai and Bi are Airy functions of the first and second kind [55], respectively. Solving Equation (22) numerically one obtains complex energies and the DC ionization rate is then given by $\Gamma_{\mathrm{DC}}(\mathsf{E}_{\mathrm{DC}}) = -2\,\mathrm{Im}\left[E(\mathsf{E}_{\mathrm{DC}})\right]$ [47, 54]. In the adiabatic regime, the ionization rate by an oscillating monochromatic field is the cycle average of the DC ionization rate corresponding to the instantaneous static electric field at a specific time $\mathsf{E}(t)$ [56], that is

$$\left\langle \Gamma_{\mathrm{Adiabatic}}(\mathsf{E}_0) \right\rangle = \frac{\omega}{2\pi} \int_0^{2\pi/\omega} \Gamma_{\mathrm{DC}}\left[\mathsf{E}(t)\right] dt. \tag{23}$$

As can be seen in the lower panel of Figure 7, this adiabatic ionization rate corresponds

exceptionally well with the average ionization rate obtained from Equation (21) with $t_0 = \pi / 2\omega$ and $n = 1$, i.e., $t \in [\pi / 2\omega; 5\pi / 2\omega]$. It should be noted here that, in this low frequency limit, ECS in both LG and VG, as well as PML in VG, diverge numerically. This phenomenon was briefly discussed above and in more detail in Ref. [23]. Thus, the low frequency ionization rate has been calculated implementing PML in LG. In general, one should choose the box size to be larger than the electron quiver amplitude E_0 / ω^2. For the low frequency in Figure 7, the largest field considered results in a quiver amplitude of 3000 a.u., which is significantly larger than the $R_0 = 20$ a.u. used in the calculation. Nevertheless, the errors introduced by the PML LG method for low frequencies are fairly low for $t \lessapprox 5\pi / 2\omega$ even with $R_0 = 20$ a.u.. Additionally, the ionization rate is not as sensitive to errors in the wave function as the error measurement in Equation (7). We are therefore able to obtain accurate ionization rates using a very small box size.

Two further comparisons are made in the lower panel of Figure 7. The first is an analytical approximation to the low frequency ionization rate. This can be obtained by analyzing the asymptotic behavior of the Airy functions. For low field strengths, $|\lambda|$ tends to infinity. In fact, both the real and imaginary part of λ tend to $+\infty$ for $\mathsf{E}_0 \to 0$. Substituting the asymptotic expressions of the Airy functions [55] into Equation (22), one obtains a polynomial in the electric field multiplied by an exponential function. Solving for the imaginary part of the energy, while retaining only first order terms in the polynomial, then leads to

$$\Gamma_{\text{asymp.}}(\mathsf{E}_{\text{DC}}) = \left(1 - \frac{5}{3}\mathsf{E}_{\text{DC}}\right) \exp\left(-\frac{2}{3\mathsf{E}_{\text{DC}}}\right). \tag{24}$$

The ionization rate of the monochromatic field can then again be obtained by Equation (23) using Equation (24) for Γ_{DC}. It can be seen to agree with the first two methods for weak fields.

The final comparison is made with the expression obtained by Perelomov, Popov, and Terent'ev (PPT) [57] for the adiabatic ionization rate for the zero-range potential in a monochromatic field with amplitude E_0

$$\left\langle \Gamma_{PPT}(E_0) \right\rangle = \left(\frac{3E_0}{\pi} \right)^{1/2} \exp\left(-\frac{2}{3E_0} \right). \tag{25}$$

It again agrees for weaker fields but as opposed to the approximation obtained by the asymptotic analysis it overestimates the ionization rate for strong fields.

VI. Excitons in Carbon nanotubes

While the zero-range potential above is very useful for probing the accuracy of PMLs in laser-matter interactions, it does not represent any physical system. In this section, we are interested in computing dissociation rates for excitons in CNTs, and in so doing analyze the errors introduced by PMLs and ECS for a more realistic potential. To describe excitons from first principles, one must solve the many-body Bethe-Salpeter equation, which is a computationally tedious task even for simple structures. Following previous work on excitons in CNTs [5, 58], we model the excitons as electron-hole pairs confined to the surface of an infinitely long cylinder of radius r. By expressing the problem in terms of the relative coordinate $\boldsymbol{r}_{eh} = \boldsymbol{r}_e - \boldsymbol{r}_h$ of the electron-hole pair, an equation that is mathematically similar to the single electron Schrödinger equation may be obtained. The separation between the electron and hole may then be written as

$$d = \sqrt{x^2 + 4r^2 \sin^2\left(\frac{\phi}{2}\right)}, \tag{26}$$

where r is the CNT radius, x is the electron-hole separation along the long axis, and ϕ the angular separation around circumference of the cylinder. If the radius of the nanotube is

sufficiently small, then it is a reasonable approximation to average the interaction between the electron and hole around the circumference of the cylinder. For a screened Coulomb interaction, this leads to [58, 59]

$$V(x) = -\frac{1}{2\pi r}\int_0^{2\pi} \frac{1}{\varepsilon\sqrt{x^2 + 4r^2\sin\left(\frac{\phi}{2}\right)}} r\,d\phi$$

$$= -\frac{2}{\pi|x|\varepsilon} K\left(-\frac{4r^2}{x^2}\right), \tag{27}$$

where ε the dielectric constant and K is complete elliptical integral of the first kind [55]. This potential diverges logarithmically for $x \to 0$ and approaches a screened Coulomb potential $V(x) = -|\varepsilon x|^{-1}$ in the limit $x \to \infty$. It does therefore not have the cut-off spatial behavior found for the zero-range potential in the previous section. The CNT excitons may then be described by the one-dimensional equation

$$i\frac{d}{dt}\psi(x,t) = \left[-\frac{1}{2\mu}\frac{d^2}{dx^2} + H_g(x,t) + V(x)\right]\psi(x,t), \tag{28}$$

where μ is the reduced mass and H_g again describes the interaction with the laser field. It is convenient to define a different set of units [5] which will be referred to as exciton units (e.u.). Whereas in atomic units one measures length and energy in Bohr radii $a_0 \approx 0.529\,\text{Å}$ and Hartrees $E_h \approx 27.2$ eV, they are measured as $a_0^* = \varepsilon a_0/\mu$ and $E_h^* = \mu E_h/\varepsilon^2$ in exciton units. The units of time and electric field strength therefore become $\hbar/E_h^*$ and E_h^*/ea_0^*, respectively, where e is the elementary charge. The advantage of using exciton units is that μ and ε are eliminated from Equation (28), which allows computation of quite general results using only a single non-trivial parameter r. Furthermore, it turns out that the radius r measured in exciton units is approximately 0.1 e.u., regardless of the chiral index of the CNT [5]. A CNT radius of $r = 0.1$

e.u. will therefore be used throughout. Such a CNT supports an exciton ground state with energy $E_0 \approx -3.9$ e.u..

A. Error analysis

We will begin by analyzing the error σ as a function of absorption width d after propagating the ground state for $t = 50$ e.u. in a field with amplitude $E_0 = 2.23$ e.u. and frequency $\omega = 1$ e.u.. These errors are shown in fig:errorvsPMLHydr for the PML method and in Figure 9 for ECS. It is clear from the previous section that a low absorption coefficient σ_0 is preferable, and therefore $\sigma_0 \in [0.001, 0.01, 0.1]$ will be used for the CNT potential. Similar trends are observed as for the zero-range potential: the quadratic absorption function with the lowest σ_0 again introduces the lowest error, but the error converges slower than for, e.g., the cubic absorption function. The two power functions with a low absorption coefficient clearly outperform the other functions. Upon comparing the errors introduced by PMLs to those introduced by ECS in Figure 9, it is evident that the PML method again introduces lower errors for comparable absorption widths and properly chosen absorption functions. One may be tempted to reduce the ECS errors by simply choosing a lower θ. However, already at $\theta = 0.1$ an absorption width of $d \approx 25$ e.u. is required for convergence to an error of around 2.3×10^{-10}, whereas PMLs with $d = 25$ e.u., $\sigma_0 = 0.001$ and a quadratic absorption function yield an error of around 2.2×10^{-13}. If a cubic absorption function is used instead, an error of around 1.4×10^{-12} is obtained already at $d = 15$ e.u..

By simply analyzing the error at $t = 50$ e.u., it seems the PML method far outperforms the ECS method. Nevertheless, the results are not as clear when analyzing the errors as a

function of time. Figure 10 shows the errors introduced by propagating the ground state in the same field, but sampled at every $t = 10$ e.u.. Additionally, two differently sized physical domains are considered. One with the absorbing layers placed at $R_0 = 10$ e.u. (dashed) and another with $R_0 = 20$ e.u. (solid). For the larger physical domain, PML VG introduces the lowest errors for $t \leq 50$ e.u.. It does, however, grow quite rapidly as the propagation time increases. This growth is even more pronounced for the smaller physical domain ($R_0 = 10$ e.u.), where it becomes larger than the errors for both ECS LG and ECS VG at $t = 50$ e.u.. As the ideal absorbing layer is not this sensitive to the position of the layers nor propagation time, PMLs implemented in FDTD scheme do not seem promising for potentials that reach into the absorbing layers.

B. Exciton dissociation in CNTs

We now turn to discussing exciton dissociation in CNTs induced by a laser field. Unlike the zero-range potential used in the previous section, the CNT potential supports many bound states, some of which have large exciton radii. In principle, all of these states must be included in Equation (18) to obtain (numerically) exact dissociation probabilities. Nevertheless, the dissociation rate may be approximated by including only the first few states in the sum, as the higher excited states dissociate much faster than these states. The first three states have energies -3.9, -0.46, and -0.26 e.u., respectively, and are sufficiently localized that a small physical domain with $R_0 = 20$ e.u. may be used. The approximate dissociation rate is shown in Figure 11, and it has been checked that all four methods yield identical results. It should be mentioned that the reason that the PML results are graphically indistinguishable from the ECS results, even though the error in the PML wave function is quite large (see Section VI A), is that the overlap

integrals in Equation (18) are not sensitive to small variations in the wave function. The largest errors in the wave function are found near the edge of the physical domain. In this region, the three states considered are very close to zero, and the product $\varphi_b^* \psi$ will therefore remain small in this region, leading to almost identical integrals. If, however, an observable that is sensitive to the details of the wave function is desired, a much larger box size will be required. The vector potential used in the calculation has been turned on smoothly over three optical cycles with $\omega = 1$ e.u., and the depletion rate has then been computed using Equation (21) with $n = 4$, i.e., averaging the time dependent dissociation rate over four optical cycles. The reason for averaging over such a large number of periods is that one obtains a much more detailed spectrum. For example, the local minimum around $E_0 = 1.9$ e.u. is not present when averaging over two periods. It is clear that certain field strengths lead to much larger dissociation rates than others, which suggests the possibility of tuning the laser amplitude to optimize dissociation. It is common to attribute the local extrema to the ponderomotive energy E_p, which is the cycle-averaged quiver energy of a free electron in a monochromatic laser field $E_p = E_0^2 / 4\omega^2$. By assuming that the energy required to dissociated the exciton is $|E_0| + E_p$, dissociation is only possible with N photons if $N\omega$ is larger than this energy. The first and second vertical dashed line in fig:CNTGSdep correspond to solutions of

$$|E_0| + \frac{E_0^2}{4\omega^2} = N\omega, \tag{29}$$

where $N = 4$ and $N = 5$, respectively. Thus, dissociation by four photons is only possible for $E_0 \lessapprox 0.58$ e.u. and five photon dissociation for $E_0 \lessapprox 2.1$ e.u. However, as can be seen in Figure 11, the ponderomotive energy does not correspond very well with the local extrema in the dissociation rate. Of course, one cannot expect a full agreement from a classical quantity.

Furthermore, during the turn-on period, the electric field is not a monochromatic field. To obtain a detailed prediction of the shape of the dissociation rate, one must therefore turn to the full numerical calculation.

VII. Concluding Remarks

We have presented a simple FDTD scheme implementing PMLs to solve the time-dependent Schrödinger equation. The method introduces absorbing layers designed to absorb outgoing probability flux while retaining the exact solution inside a box of some desired size. The performance of the method is compared to the well known ECS method. It is observed that the PMLs implemented in VG introduce errors that are much lower than those introduced by ECS when they are implemented for short-range potentials. On the other hand, when the potential reaches into the absorbing domain, the PMLs do not function as proper absorbing layers, since the errors are very sensitive to the location of the layers, as well as the propagation time. This effect is not observed in ECS, and it is therefore safer to use ECS for long-range potentials. The methods have subsequently been used to compute the laser induced ionization rate of an electron initially bound to a zero-range potential, as well as exciton dissociation rates in CNTs. In both cases, a pronounced dependence on the field amplitude was observed, which is to be expected. The ionization and dissociation rates, furthermore, show many local minima and maxima as a function of field amplitude suggesting that one may induce faster exciton dissociation by optimizing the amplitude of the laser field.

ACKNOWLEDGMENTS

Useful comments from Lars Bojer Madsen are gratefully acknowledged. This work was supported by the Villum Kann Rasmussen (VKR) Center of Excellence QUSCOPE. Additionally, H.C.K. and T.G.P. are supported by the Center for Nanostructured Graphene (CNG), which is sponsored by the Danish National Research Foundation, Project No. DNRF103.

APPENDIX A: Finite Difference Formulas

The finite difference (FD) approach used in the present paper is based on the Crank-Nicolson scheme [60]. It consists of a combination of the forward (explicit) and backward (implicit) Euler method and reads

$$i\frac{\psi\left(x,t_{j+1}\right)-\psi\left(x,t_{j}\right)}{\Delta t} = \frac{1}{2}\left[H\left(t_{j+1}\right)\psi\left(x,t_{j+1}\right)+H\left(t_{j}\right)\psi\left(x,t_{j}\right)\right], \tag{A1}$$

where $t_j = j\Delta t$ and $H\left(t_j\right)$ is the Hamilton operator at time t_j. What remains is to discretize the spatial derivatives. For the PML method, the kinetic term is given by

$$T_{\mathrm{PML}} = -\frac{1}{2}c\left(x\right)\frac{\partial}{\partial x}c\left(x\right)\frac{\partial}{\partial x}\psi = -\frac{1}{2}\left[c^{2}\left(x\right)\frac{\partial^{2}\psi}{\partial x^{2}}+c\left(x\right)\frac{\partial c\left(x\right)}{\partial x}\frac{\partial\psi}{\partial x}\right]. \tag{A2}$$

Both c and its derivative are known analytically. The derivatives of the wave function are approximated using the second-order approximations

$$\frac{\partial\psi}{\partial x}\approx\frac{\psi_{n+1}-\psi_{n-1}}{2\Delta x} \tag{A3}$$

$$\frac{\partial^{2}\psi}{\partial x^{2}}\approx\frac{\psi_{n+1}-2\psi_{n}+\psi_{n-1}}{\left(\Delta x\right)^{2}}, \tag{A4}$$

with $\psi_n = \psi(x_n)$ and $x_n = n\Delta x$, where n is an integer running from $-N$ to N for a grid with a total of $2N+1$ equidistant points. These simple FD formulas are one of the advantages of the PML method.

For the ECS method, on the other hand, the transformation leads to modified FD formulas. They can be derived by writing the wave function as a standard approximation using Lagrange interpolating polynomials

$$\psi(\tilde{x}) \approx \sum_{n=-p}^{p} l_n(\tilde{x})\psi(\tilde{x}_n) \tag{A5}$$

with

$$l_n(\tilde{x}) = \prod_{\substack{m=-p \\ m\neq n}}^{p} \frac{\tilde{x}-\tilde{x}_m}{\tilde{x}_n-\tilde{x}_m}. \tag{A6}$$

The FD formulas at any particular point are then derived by differentiating Eq. (A5) and evaluating the result at said point, all the while keeping in mind Eq. (9). That is,

$$\tilde{x}_n = \begin{cases} x_n & \text{for } x_n \le R_0 \\ e^{i\theta}(x_n \pm R_0) \mp R_0 & \text{for } \mp x > R_0, \end{cases} \tag{A7}$$

where x_n is the equidistant grid described above. Here we use $p=1$, which leads to the standard FD formulas for $|x| < R_0$. Outside the scaling radius we simply pick up a complex phase factor

$$\frac{d\psi}{dx} \approx \frac{e^{-i\theta}}{2\Delta x}(\psi_{n+1}-\psi_{n-1}) \tag{A8}$$

$$\frac{d^2\psi}{dx^2} \approx \frac{e^{-i2\theta}}{(\Delta x)^2}(\psi_{n-1}-2\psi_n+\psi_{n+1}), \tag{A9}$$

while at the scaling radius we have the non-symmetric formulas

$$\frac{d\psi}{dx} \approx \frac{1}{\Delta x}\left[-\frac{e^{\pm i\theta}}{e^{i\theta}+1}\psi_{n-1} \pm \left(1-e^{-i\theta}\right)\psi_n\right.$$

$$+\frac{e^{\mp i\theta}}{e^{i\theta}+1}\psi_{n+1}\Bigg] \quad \text{for } x=\pm R_0 \tag{A10}$$

$$\frac{d^2\psi}{dx^2}\approx\frac{1}{(\Delta x)^2}\Bigg[\frac{2}{e^{i\theta}+1}\psi_{n\mp1}-2e^{-i\theta}\psi_n$$

$$+\frac{2e^{-i\theta}}{e^{i\theta}+1}\psi_{n\pm1}\Bigg] \quad \text{for } x=\pm R_0 \tag{A11}$$

As was discussed in Ref. [50], the ECS FD formulas are $O\left[(\Delta x)^2\right]$ for $x\neq\pm R_0$ but only $O(\Delta x)$ for $x=\pm R_0$. For all calculations in the present paper, we have used $\Delta x=10^{-2}$ and $\Delta t=10^{-3}$.

[1] Q. H. Wang, K. Kalantar-Zadeh, A. Kis, J. N. Coleman, and M. S. Strano, Nat. Nanotechnol. **7**, 699 (2012)

[2] A. K. Geim and I. V. Grigorieva, Nature **499**, 419 (2013)

[3] T. Olsen, S. Latini, F. Rasmussen, and K. S. Thygesen, Phys. Rev. Lett. **116**, 056401 (2016)

[4] T. Ando, J. Phys. Soc. Jpn. **66**, 1066 (1997)

[5] T. G. Pedersen, Phys. Rev. B **67**, 073401 (2003)

[6] T. G. Pedersen, Phys. Rev. B **94**, 125424 (2016)

[7] M. Massicotte, F. Vialla, P. Schmidt, M. B. Lundeberg, S. Latini, S. Haastrup, M. Danovich, D. Davydovskaya, K. Watanabe, T. Taniguchi, V. I. Falko, K. Thygesen, T. G. Pedersen, and F. H. L. Koppens, Nat. Commun. **9**, 1633 (2018)

[8] C. D. Spataru, S. Ismail-Beigi, L. X. Benedict, and S. G. Louie, Phys. Rev. Lett. **92**, 077402 (2004)

[9] V. Perebeinos, J. Tersoff, and P. Avouris, Phys. Rev. Lett. **92**, 257402 (2004)

[10] F. Wang, G. Dukovic, L. E. Brus, and T. F. Heinz, Science **308**, 838 (2005)

[11] J. Maultzsch, R. Pomraenke, S. Reich, E. Chang, D. Prezzi, A. Ruini, E. Molinari, M. S. Strano, C. Thomsen, and C. Lienau, Phys. Rev. B **72**, 241402 (2005)

[12] M. Bernardi, M. Palummo, and J. C. Grossman, Nano Lett. **13**, 3664 (2013)

[13] O. Lopez-Sanchez, E. Alarcon Llado, V. Koman, A. Fontcuberta i Morral, A. Radenovic, and A. Kis, ACS Nano **8**, 3042 (2014)

[14] S. Haastrup, S. Latini, K. Bolotin, and K. S. Thygesen, Phys. Rev. B **94**, 041401 (2016)

[15] H. C. Kamban and T. G. Pedersen, Phys. Rev. B **100**, 045307 (2019)

[16] S.-W. Chang, J. Hazra, M. Amer, R. Kapadia, and S. B. Cronin, ACS Nano **9**, 11551 (2015)

[17] V. Perebeinos and P. Avouris, Nano Lett. **7**, 609 (2007)

[18] A. Mohite, J.-T. Lin, G. Sumanasekera, and B. W. Alphenaar, Nano Lett. **6**, 1369 (2006)

[19] A. D. Mohite, P. Gopinath, H. M. Shah, and B. W. Alphenaar, Nano Lett. **8**, 142 (2008)

[20] T. Uda, M. Yoshida, A. Ishii, and Y. K. Kato, Nano Lett. **16**, 2278 (2016)

[21] U. V. Riss and H. Meyer, J. Chem. Phys. **105**, 1409 (1996)

[22] J. L. Krause, K. J. Schafer, and K. C. Kulander, Phys. Rev. A **45**, 4998 (1992)

[23] F. He, C. Ruiz, and A. Becker, Phys. Rev. A **75**, 053407 (2007)

[24] L. Tao, W. Vanroose, B. Reps, T. N. Rescigno, and C. W. McCurdy, Phys. Rev. A **80**, 063419 (2009)

[25] C. W. McCurdy, C. K. Stroud, and M. K. Wisinski, Phys. Rev. A **43**, 5980 (1991)

[26] A. Scrinzi, Phys. Rev. A **81**, 053845 (2010)

[27] J.-P. Berenger, J. Comput. Phys. **114**, 185 (1994)

[28] U. S. Inan and R. A. Marshall, *Numerical Electromagnetics - The FDTD Method* (Cambridge University Press, New York, USA, 2011)

[29] S. C. Hagness and A. Taflove, *Computational Electrodynamics: The Finite Difference Time Domain Method* (Artech House, Norwood, USA, 2005)

[30] J. Jin, *The Finite Element Method in Electromagnetics, 2nd edition* (Wiley-Interscience, Hoboken , New Jersey, USA, 2002)

[31] D. Zhang, H. Jia, and K. Yasumoto, Int. J. Infrared. Milli. **29**, 823 (2008)

[32] Y. Y. Lu and J. Zhu, IEEE Photonics Technol. Lett. **17**, 2601 (2005)

[33] P. Zuo and Z. Fan, J. Sound Vib. **406**, 181 (2017)

[34] C. Zheng, J. Comput. Phys. **227**, 537 (2007)

[35] A. Nissen and G. Kreiss, Commun. Comput. Phys. **9**, 147179 (2011)

[36] A. Nissen, H. O. Karlsson, and G. Kreiss, J. Chem. Phys. **133**, 054306 (2010)

[37] L. Lehtovaara, V. Havu, and M. Puska, J. Chem. Phys. **135**, 154104 (2011)

[38] O. Pinaud, J. Comput. Phys. **289**, 169 (2015)

[39] T. G. Pedersen, Phys. Lett. A **379**, 1785 (2015)

[40] G. Scharf, K. Sonnenmoser, and W. F. Wreszinski, Phys. Rev. A **44**, 3250 (1991)

[41] E. Balslev and J. M. Combes, Commun. Math. Phys. **22**, 280 (1971)

[42] J. Aguilar and J. M. Combes, Commun. Math. Phys. **22**, 269 (1971)

[43] G. D. Doolen, J. Nuttal, and R. W. Stagat, Phys. Rev. A **10**, 1612 (1974)

[44] Y. K. Ho, Phys. Rev. A **23**, 2137 (1981)

[45] M. Reed and B. Simon, *Methods of Modern Mathematical Physics* (Academic, New York, 1982)

[46] J. Bengtsson, E. Lindroth, and S. Selstø, Phys. Rev. A **78**, 032502 (2008)

[47] I. W. Herbst and B. Simon, Phys. Rev. Lett. **41**, 67 (1978)

[48] T. G. Pedersen, H. Mera, and B. K. Nikolić, Phys. Rev. A **93**, 013409 (2016)

[49] B. Simon, Phys. Lett. A **71**, 211 (1979)

[50] C. W. McCurdy, M. Baertschy, and T. N. Rescigno, J. Phys. B **37**, R137 (2004)

[51] T. N. Rescigno and C. W. McCurdy, Phys. Rev. A **62**, 032706 (2000)

[52] A. Bermúdez, L. Hervella-Nieto, A. Prieto, and R. Rodríguez, C. R. Math. Acad. Sci. Ser. A **339**, 803 (2004)

[53] B. J. Postma, Am. J. Phys. **52**, 725 (1984)

[54] F. M. Fernández and E. A. Castro, Am. J. Phys. **53**, 757 (1985)

[55] M. Abramowitz and I. Stegun, eds., *Handbook of Mathematical Functions, With Formulas, Graphs, and Mathematical Tables* (Dover, New York, 1972)

[56] C. J. Joachain, N. J. Kylstra, and R. M. Potvliege, *Atoms in Intense Laser Fields* (Cambridge University Press, Cambridge, UK, 2011)

[57] A. Perelomov, V. Popov, and M. Terent'ev, Sov. Phys. JETP **23**, 924 (1966)

[58] T. F. Rønnow, T. G. Pedersen, and H. D. Cornean, Phys. Lett. A **373**, 1478 (2009)

[59] T. G. Pedersen, K. Pedersen, H. D. Cornean, and P. Duclos, Nano Lett. **5**, 291 (2005)

[60] J. Crank and P. Nicolson, Adv. Comput. Math. **6**, 207 (1996)

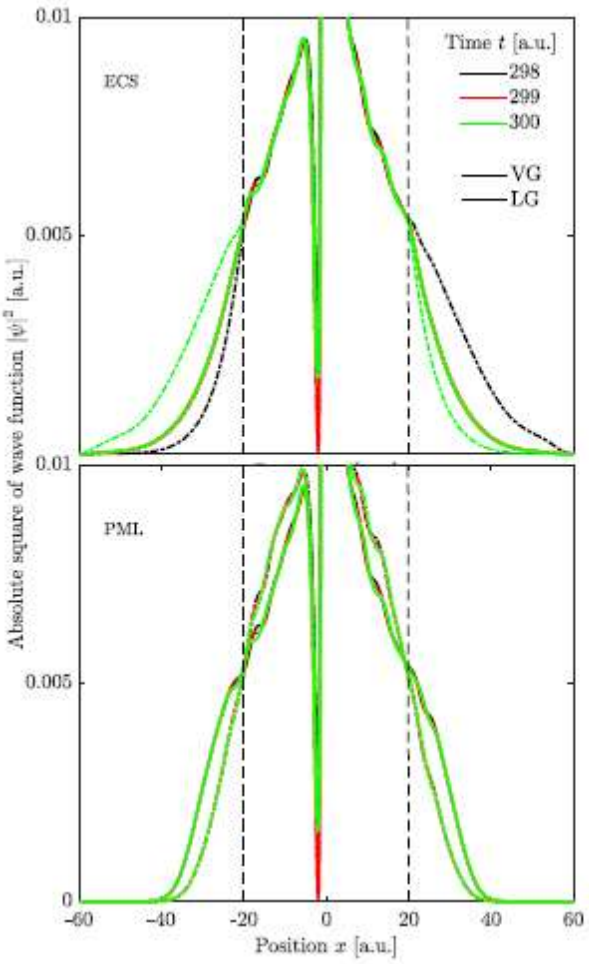

FIG. 1. Absolute square of wave functions calculated with ECS (upper) and PML (lower) for three different times with $R_0 = 20$ a.u. (indicated by vertical dashed lines). The solid and dash-dotted lines are calculated in VG and LG, respectively. The field parameters are $E_0 = 0.1$

a.u. and $\omega = 0.52$ a.u., and the field has been turned on smoothly over three optical cycles.

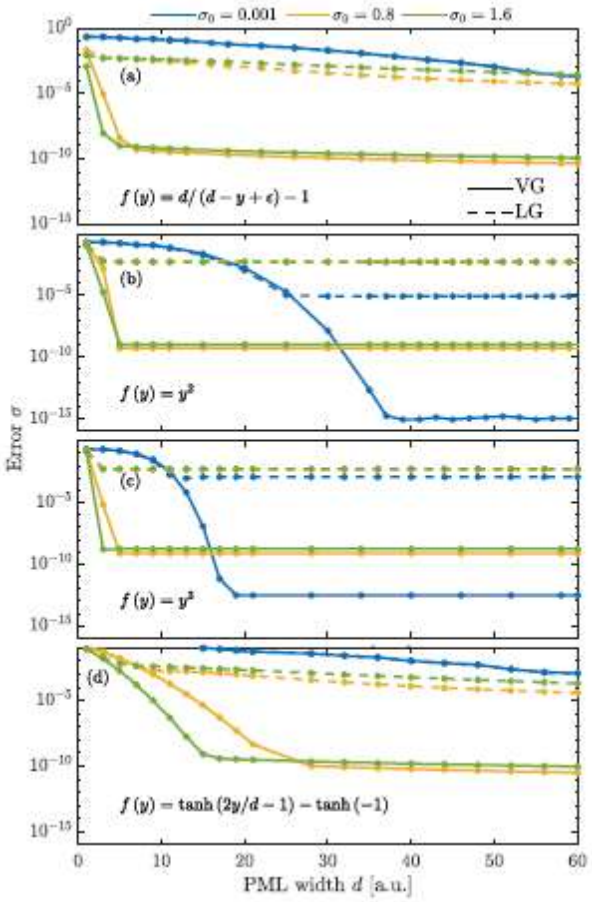

FIG. 2. Error at $t = 200$ a.u. as a function of PML width for four different absorption functions and various absorption coefficients. The solid and dashed lines correspond to PML VG and LG, respectively. The scaling radius is set to $R_0 = 20$ a.u.. The field parameters are the same as in Figure 1.

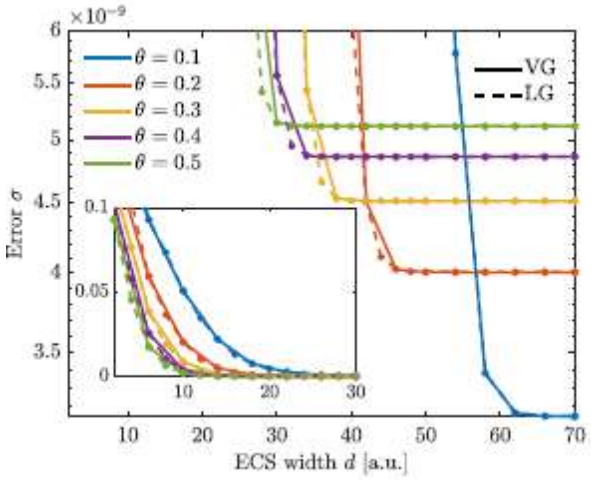

FIG. 3. Error at $t = 200$ a.u. as a function of ECS width for various angles of rotation. The field parameters are the same as in Figure 1. The inset shows the behavior for smaller widths.

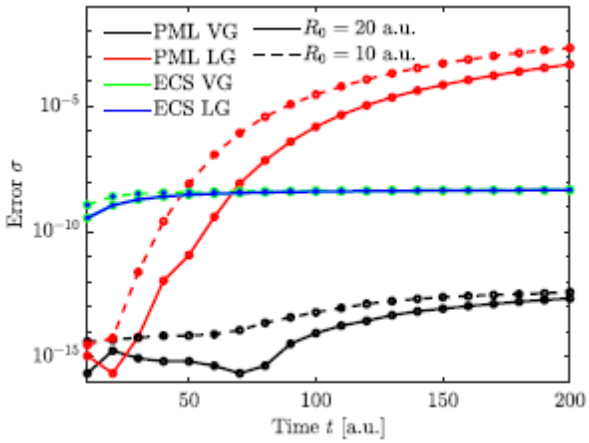

FIG. 4. Error as a function of time. The absorbing boundary is located at $R_0 = 20$ and at $R_0 = 10$ a.u. for the solid and dashed lines, respectively. The PML calculations have been made with $\sigma_0 = 0.001$ and the cubic absorption function, while the ECS calculations have been made with $\theta = 0.35$. In both cases the absorption width is $d = 40$ a.u.. The field parameters are the same as in Figure 1.

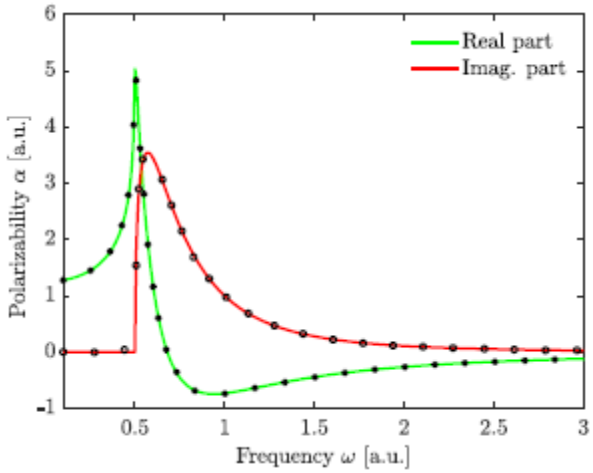

FIG. 5. Polarizability calculated from first order perturbation theory (solid lines) and the PML method (markers). A field strength of $E_0 = 10^{-6}$ a.u. was used.

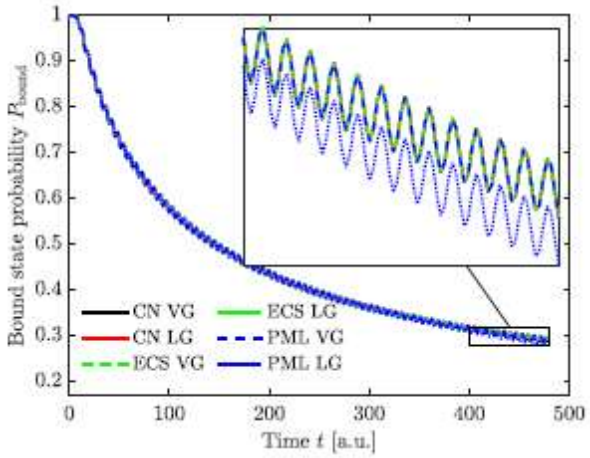

FIG. 6. Probability of occupying a bound state as a function of time. The results obtained with absorbing layers (ECS and PML) are compared to those obtained with the Crank-Nicolson (CN) scheme without any absorbing layers. The field parameters are the same as in fig:WFSW and has been turned on smoothly over one optical cycle.

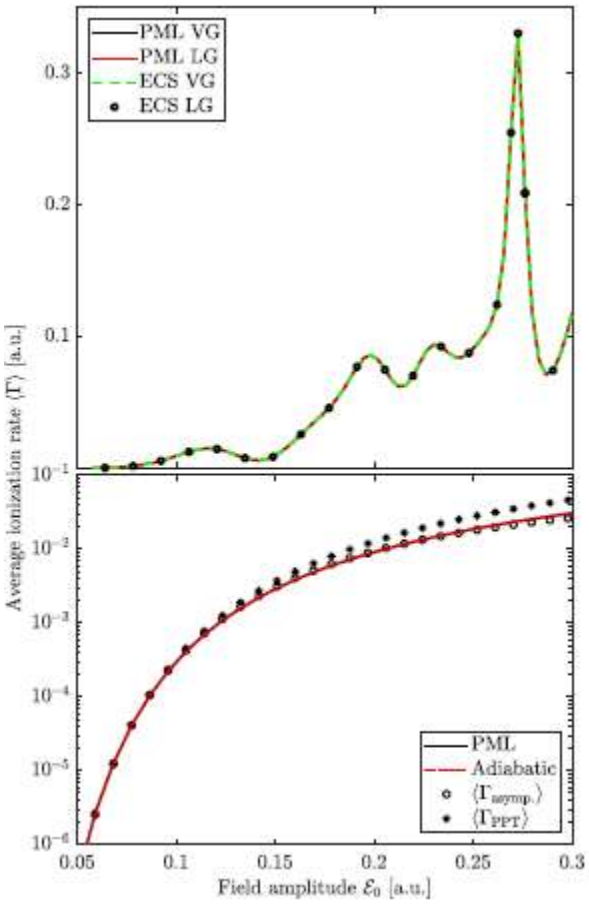

FIG. 7. Ionization rate for $\omega = 0.2$ a.u. (upper) and $\omega = 0.01$ a.u. (lower). For the larger frequency, the vector potential has been turned on smoothly over $t = 35$ a.u., while for the lower frequency the electric field has been turned on linearly over the same amount of time. The ionization rate in Eq. (20) has been averaged over $[4\pi/\omega; 8\pi/\omega]$ for the larger frequency, and over $[\pi/2\omega; 5\pi/2\omega]$ for the lower frequency.

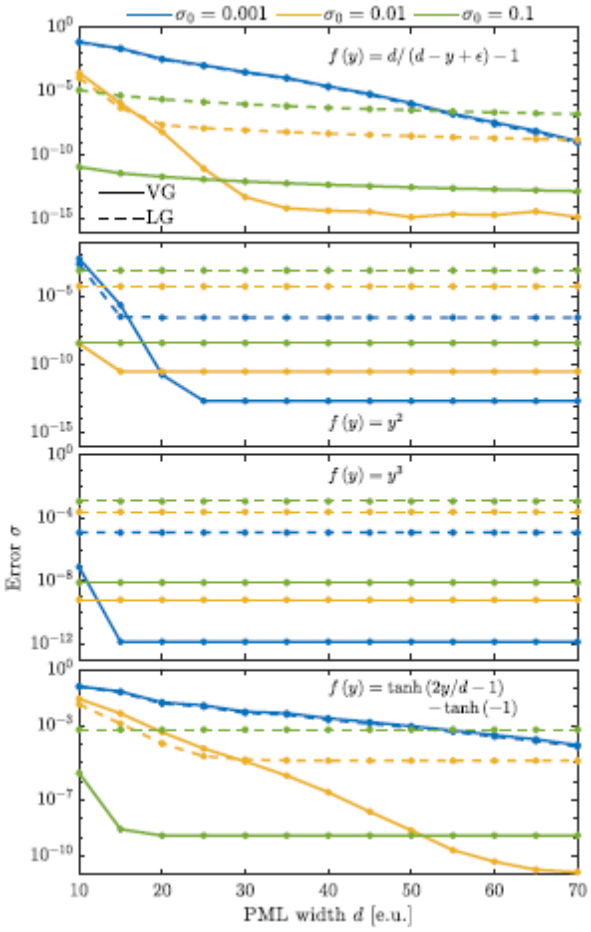

FIG. 8. Error at time $t = 50$ e.u as a function of PML width for four different absorption functions and various absorption coefficients. The solid and dashed lines correspond to PML VG and LG, respectively. The field parameters are $E_0 = 2.23$ e.u. and $\omega = 1$ e.u., and it has been turned on smoothly over three optical cycles.

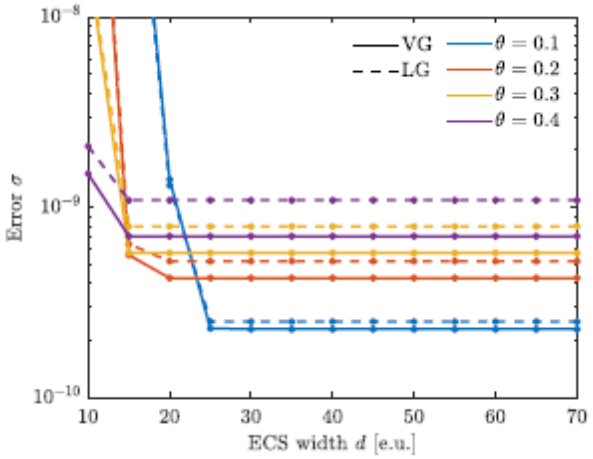

FIG. 9. Error at time $t = 50$ e.u. as a function of ECS width for various angles of rotation. The field parameters are the same as in Figure 8.

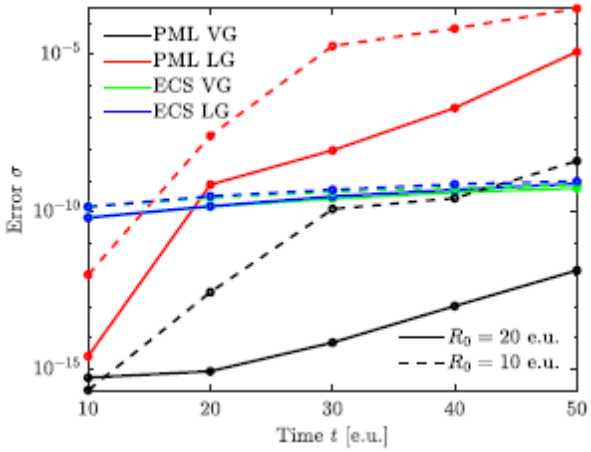

FIG. 10. Error as a function of time. The absorbing boundary is located at $R_0 = 20$ e.u. and $R_0 = 10$ e.u. for the solid and dashed lines, respectively. The PML calculations have been made with $\sigma_0 = 0.001$ and the cubic absorption function, while the ECS calculations have been made with $\theta = 0.3$. In both cases the absorption width is $d = 20$ e.u.. The field parameters are the same as in Figure 8.

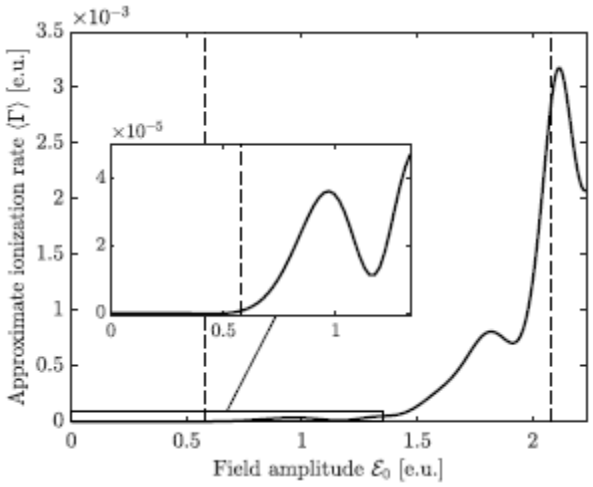

FIG. 11. Exciton dissociation rate for $\omega = 1$ e.u.. The vector potential has been turned on smoothly over three optical cycles, and the depletion rate has been averaged over two optical cycles (after the field has been turned on).

Summary

A Finite-Difference Time-Domain scheme with Perfectly Matched Layers has been introduced for solving the time-dependent Schrödinger equation, and simulate the laser induced ionization of two systems: (i) an electron initially bound to a one-dimensional zero-range potential, and (ii) excitons in carbon nanotubes.